

Active learning for effective Hamiltonian of super-large-scale atomic structures

Xingyue Ma,^{1,2} Hongying Chen,^{1,2} Ri He,³ Zhanbo Yu,^{1,2} Sergei Prokhorenko,⁴ Zheng Wen,⁵ Zhicheng Zhong,^{3,6} Jorge Iñiguez,⁷ L. Bellaiche,⁴ Di Wu,^{1,2} and Yurong Yang^{1,2}

¹*National Laboratory of Solid State Microstructures and Collaborative Innovation Center of Advanced Microstructures, Nanjing University, Nanjing 210093, China*

²*Jiangsu Key Laboratory of Artificial Functional Materials,*

Department of Materials Science and Engineering, Nanjing University, Nanjing 210093, China

³*Key Laboratory of Magnetic Materials Devices & Zhejiang Province Key Laboratory of Magnetic Materials and Application Technology, Ningbo Institute of Materials Technology and Engineering, Chinese Academy of Sciences, Ningbo 315201, China*

⁴*Physics Department and Institute for Nanoscience and Engineering,*

University of Arkansas, Fayetteville, Arkansas 72701, USA

⁵*College of Electronics and Information, Qingdao University, Qingdao, 266071, China*

⁶*China Center of Materials Science and Optoelectronics Engineering,*

University of Chinese Academy of Sciences, Beijing 100049, China

⁷*Materials Research and Technology Department, Luxembourg Institute of Science and Technology (LIST),*

Avenue des Hauts-Fourneaux 5, L-4362 Esch/Alzette, Luxembourg

(Dated: March 20, 2024)

The first-principles-based effective Hamiltonian is widely used to predict and simulate the properties of ferroelectrics and relaxor ferroelectrics. However, the parametrization method of the effective Hamiltonian is complicated and hardly can resolve the systems with complex interactions and/or complex components. Here, we developed an on-the-fly active machine learning approach to parametrize the effective Hamiltonian based on Bayesian linear regression. The parametrization is completed in molecular dynamics simulations, with the energy, forces and stress predicted at each step along with their uncertainties. First-principles calculations are executed when the uncertainties are large to retrain the parameters. This approach provides a universal and automatic way to compute the effective Hamiltonian parameters for any considered systems including complex systems which previous methods can not handle. The form of the effective Hamiltonian is also revised to include some complex terms. BaTiO_3 , CsPbI_3 and $\text{SrTiO}_3/\text{PbTiO}_3$ surface are taken as examples to show the accurateness of this approach comparing with conventional first-principles parametrization method.

First-principles (FP) methods based on density functional theory (DFT) is a powerful tool for science research in physics, chemistry, materials and other fields [1]. However, studying the structure and properties at finite temperature, such as the phase transitions induced by temperature, remains a great challenge due to the large computational cost using *ab initio* molecular dynamics. Thanks to the machine learning technology, the molecular dynamics with first-principles-based machine learning force fields (MLFFs) is recently successfully used in many materials [2–6]. By these MLFFs methods, the studied system can be as large as tens thousand of atoms or even larger, however the mechanism picture (physical meanings and changes of the order parameters) may be not clear. Moreover, to make the MLFFs feasible, all MLFF approaches learn only *local* environments of atoms within a cutoff radius ($< 1 \text{ nm}$). The locality resulted in MLFFs are inherently short-ranged. The lack of long-range interactions in MLFFs can lead to both quantitative and qualitative errors, especially when describing nanopolar regions in relaxor ferroelectrics. To conveniently study the mechanism or properties at finite temperature, the first-principles-based effective Hamiltonian approach was proposed, where the Hamiltonian describes the order-parameter couplings (both long-ranged and short-ranged) and the corresponding coupling parameters are computed by first principles [7, 8], which has been successfully used for a large number of materials, such as BaTiO_3 [7], $\text{Pb}(\text{Zr}, \text{Ti})\text{O}_3$ [9], KNbO_3 [10],

CsPbI_3 [11] and so on. Monte Carlo (MC) and molecular dynamics (MD) simulations based on the effective Hamiltonian have successfully reproduced or predicted phase transitions [12], topological defects [13], dielectric response [14], piezoelectric effect [15], electrocaloric effect [16], optical response [10], and the effect of atomic ordering [17].

The effective Hamiltonian is built up based on the Taylor expansion of small structural distortions with energy around a selected high symmetry reference structure, and the expansion parameters of order-parameter coupling are typically fitted by performing FP calculations for many structures with special structure distortions [7, 18]. The fitting and verifying of these parameters for order-parameter coupling are tricky and complex, especially for systems with complex interactions. Additional manual adjusting the values of some parameters may be necessary to reproduce some experimental results correctly [10, 11], which may be resulted from the large uncertainty arisen from the parametrization process [10]. Moreover, for complex structures, such as perovskites with multi elements in *A* or *B* sites [e.g. $(\text{Ba}, \text{Sr})\text{TiO}_3$ and $\text{Pb}(\text{Zr}, \text{Ti})\text{O}_3$], the effective Hamiltonian is usually built up by applying virtual crystal approximation and a small amount of simple terms that dependent explicitly on the atomic distributions [19, 20]. For most complex system, this approximation fails to mimic the structures and properties. Therefore, the failure of approximations and trickiness of parametrization largely limit the implementation of the effective Hamiltonian methods for complex sys-

tem.

Very interesting phenomena in complex system, such as polar vortices [21], ferroelectric labyrinthine domains [22], polar skyrmion [23] and merons, were recently found [24]. Though effective Hamiltonian studies of these new phenomena for relative simple system were performed, modeling some complex materials [25] by the effective Hamiltonian is beyond the capability of currently available effective Hamiltonian model and parametrization methods. Thus, finding a new scheme for fitting the parameters of effective Hamiltonian in a reliable and automatic way is highly demanded.

In this article, on-the-fly active learning method is applied to the parametrization of a general effective Hamiltonian for complex system, and perovskite structures with multi A- or B-site elements are taken as examples. The mimic results from machine learning methods are consistent very well with other first-principles-based calculations and experiments. Such highly-automatic approach provides a way to determine the effective Hamiltonian parameters reliably, making it possible to parametrize complex interactions for possible complex systems. Our scheme largely expands the application of the effective Hamiltonian for various structures and provides a powerful tool for non-specialized scientist to mimic structures, properties, and complex phenomena.

RESULTS

Effective Hamiltonian

The effective Hamiltonian describes the couplings between order parameters, here it is developed based on the Taylor expansion of small distortions around the reference structure. Various order parameters (or “mode” distortions comparing to the reference structure) are considered (see Fig. 1a for an example), which is further explained in “Methods”. Briefly, the degrees of freedom of the effective Hamiltonian are: (1) several local modes sitting on each unit cell i , to be denoted as $\{s_1\}, \{s_2\}, \dots$, representing atomic displacements of different modes; (2) the (homogeneous) strain tensor η [7]; and (3) the variable $\{\sigma\}$ representing the atom occupation in unit cell i [for example, in $\text{Pb}(\text{Sc}, \text{Ta})\text{O}_3$, $\sigma_i = 1$ (respectively, $\sigma_i = 2$) represents a Sc (respectively, Ta) atom sitting in unit cell i] [19]. The potential energy contains four main parts

$$\begin{aligned} E_{\text{pot}} = & E_{\text{single}}(\{s_1\}, \{s_2\}, \dots) + \\ & E_{\text{strain}}(\{s_1\}, \{s_2\}, \dots, \eta) + \\ & E_{\text{conv}}(\{s_1\}, \{s_2\}, \dots) + \\ & E_{\text{spring}}(\{s_1\}, \{s_2\}, \dots, \{\sigma_i\}), \end{aligned} \quad (1)$$

where E_{single} contains the self energies of each mode, which involves only one site in each term, E_{strain} contains all the energy terms that directly related to the strain tensor η , E_{conv} contains several terms that take the “convolution” form, describing the two-body interactions between order parameters of different types or at different sites, and E_{spring} describes the

effect of atomic configuration of different elements (known as “alloying effect” [19]), which consists of several “spring” terms (using the terminology of Ref. [26]).

The forms of E_{single} and E_{strain} are basically the same as that used in previous works (see, e.g., Refs. [7, 11]), while E_{conv} and E_{spring} here is different from previous works (see, e.g., Refs. [9, 27, 28]). Such terms are derived from symmetry here, making them more general, and the accuracy of the effective Hamiltonian could be easier to be improved systematically.

The MD simulations are performed with the effective Hamiltonian by solving the equation of motions of each degree of freedom

$$\begin{aligned} \frac{\partial p_i}{\partial t} &= -\frac{\partial E_{\text{pot}}}{\partial s_i}, \\ \frac{\partial s_i}{\partial t} &= \frac{p_i}{m_i}, \end{aligned} \quad (2)$$

where p_i and m_i are the momentum and effective mass associated with the degree of freedom s_i , respectively; and t is the time.

In principle, the formalism of effective Hamiltonian could be applied to any proper ferroelectric materials that could be interpreted using the soft mode theory. Here, we mainly focus on the perovskites in formula ABX_3 , with multiple elements occupying the A - or B -site. Practically, the soft mode vector $\{u\}$, antiferrodistortive (AFD) pseudovector $\{\omega\}$ and anharmonic strain vector (acoustic mode) $\{v\}$ are considered as the modes $\{s\}$ (see Fig. 1a). More details of the effective Hamiltonian for perovskites are described in “Methods”.

Formalism of the parametrization

Instead of doing lots of energy calculations on special structures with distortion from first principles to compute the parameters of order-parameters coupling in effective Hamiltonian in previous reports [7, 18], we use the on-the-fly machine learning approach to automatically compute the parameters for effective Hamiltonian. Except the parameters directly related to the long-range dipolar interaction E_{long} [Eq. (7) in Methods] [i.e. the lattice constant a_0 , the soft mode Born effective charge Z^* and optical dielectric constant ϵ_∞ (using the notations of Ref. [7])] are determined from the first principles calculations, all the other parameters are determined through on-the-fly machine learning process. It is clear (see Methods) that the effective Hamiltonian could be written in the following form

$$E_{\text{pot}} = E_{\text{long}} + \sum_{\lambda=1}^M w_\lambda t_\lambda(\{u\}, \{v\}, \{\omega\}, \{\sigma\}, \eta), \quad (3)$$

where E_{long} is fixed during the fitting process, M is the number of parameters to be fitted, w_λ is the parameter to be fitted, and t_λ is the energy term dependent on the parameter w_λ ,

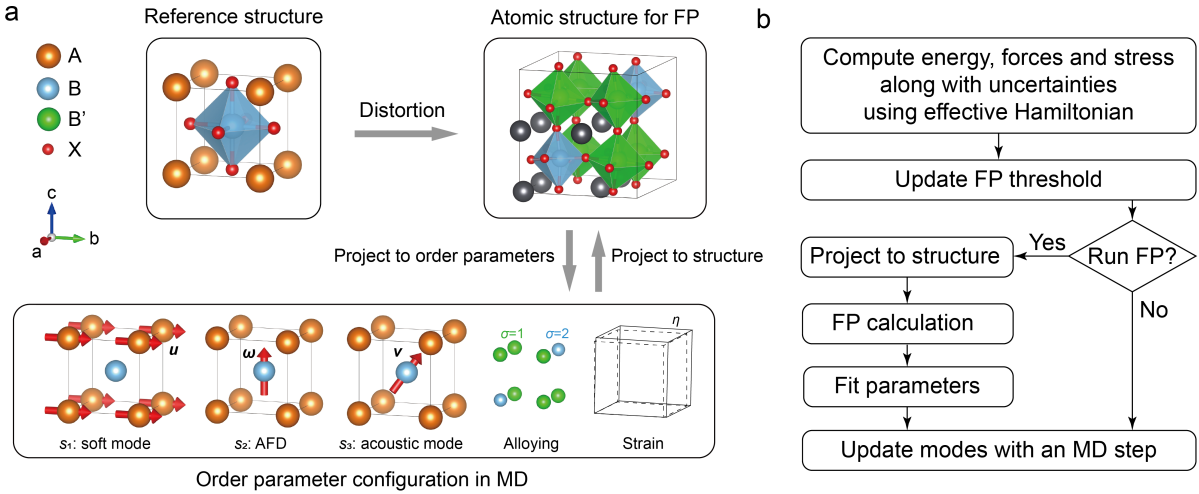


FIG. 1. Schematics of on-the-fly learning of effective Hamiltonian for perovskite structure. (a) The projection between the atomic structure used in the FP calculations and the order-parameters configuration used in effective Hamiltonian MD simulations. (b) The workflow of on-the-fly learning of effective Hamiltonian.

which is called symmetry-adapted term (SAT), using the terminology of Refs. [29]. In other words, the energy apart from the long-range dipolar energy is *linearly* dependent on the *parameters*. Moreover, it is clear that the force (respectively, stress) have similar forms to the energy, which is obtained by taking derivative over mode (respectively, strain) on E_{long} and t_λ . Such linearity is similar to the second-principle lattice dynamics [29] and MLFF with Gaussian approximation potential [30], allowing the application of similar regression algorithms. Here, we use the Bayesian linear regression algorithm similar to that previously used for MLFF [2], with several key modifications for the effective Hamiltonian context.

Given the linearity above, the energy, force and stress for each structure a calculated from the effective Hamiltonian could be written in the following matrix form

$$\tilde{\mathbf{y}}_a \equiv \mathbf{y}_a - \mathbf{y}_a^{\text{long}} = \phi_a \mathbf{w}, \quad (4)$$

where \mathbf{y} is a vector containing the energy per unit cell with respect to the reference structure, the forces acting on the modes and the stress tensor (in total $m_a = 1 + 9N + 6$ elements), \mathbf{y}^{long} is a vector in similar layout associated with the E_{long} term, and \mathbf{w} is a vector consists of all the parameters w_λ , $\lambda = 1, \dots, M$; and ϕ_a is an $m_a \times M$ matrix consists of the SAT and its derivatives with respect to modes and strain. Note that in the effective Hamiltonian formalism, the potential energy of the reference structure is zero by definition. Thus, the energy obtained from the FP calculations in \mathbf{y} should be subtracted by the energy of the reference structure to be consistent with the effective Hamiltonian.

In the parametrization process, a set of structures are selected as the training set, and the structures are indexed by $a = 1, \dots, N_T$. First-principles calculations are performed on these structures to get the energy per unit cell, forces acting on the atoms, and stress tensor. The forces acting on the modes are then obtained by applying Eq. (17) (more details

are described ‘Mode and basis’ in Methods). The $\tilde{\mathbf{y}}_a$ vector of all the structures in the training set then constitute the vector \mathbf{Y} containing $\sum_a m_a$ elements. On the other hand, the ϕ_a matrices of the structures in the training set constitute the Φ matrix. In this form, the parametrization problem is to adjust \mathbf{w} to fit $\Phi \mathbf{w}$ against \mathbf{Y} . To balance the energy, force and stress values with different dimensions properly, they are typically divided by their standard deviation in the training set to get dimensionless values. Furthermore, an optional weight could be assigned to each of the types to adjust the preference between different fitting targets. Practically, this is achieved by left multiplying a diagonal matrix \mathbf{H} made up by h_i/σ_i to Φ and \mathbf{Y} , where h_i and σ_i are the weight and standard deviation of the specified type of values (energy, force of different modes and stress), respectively. Note that the parameters in E_{spring} in Eq. (1) which are explicitly dependent on the atomic distributions ($\{\sigma_i\}$) are treated in a similar manner to other parameters. More details are provided in ‘Multi A- or B-site element perovskites’ in Supplementary Information.

Once the training set is supplied, the parameters as well as their uncertainties could be predicted with the Bayesian linear regression (see ‘Bayesian linear regression’ in Methods). Moreover, for a new structure that is not contained in the training set (i.e. FP calculation is *not* performed on such structure), the energy, forces and stress could be predicted by the regression model along with their uncertainties. Such uncertainties are used to determine whether FP calculation is necessary for such structure.

On-the-fly learning

In our approach, the parameters of effective Hamiltonian are fit in a scheme similar to that generating on-the-fly machine learning force field (MLFF) [2] with some modifications

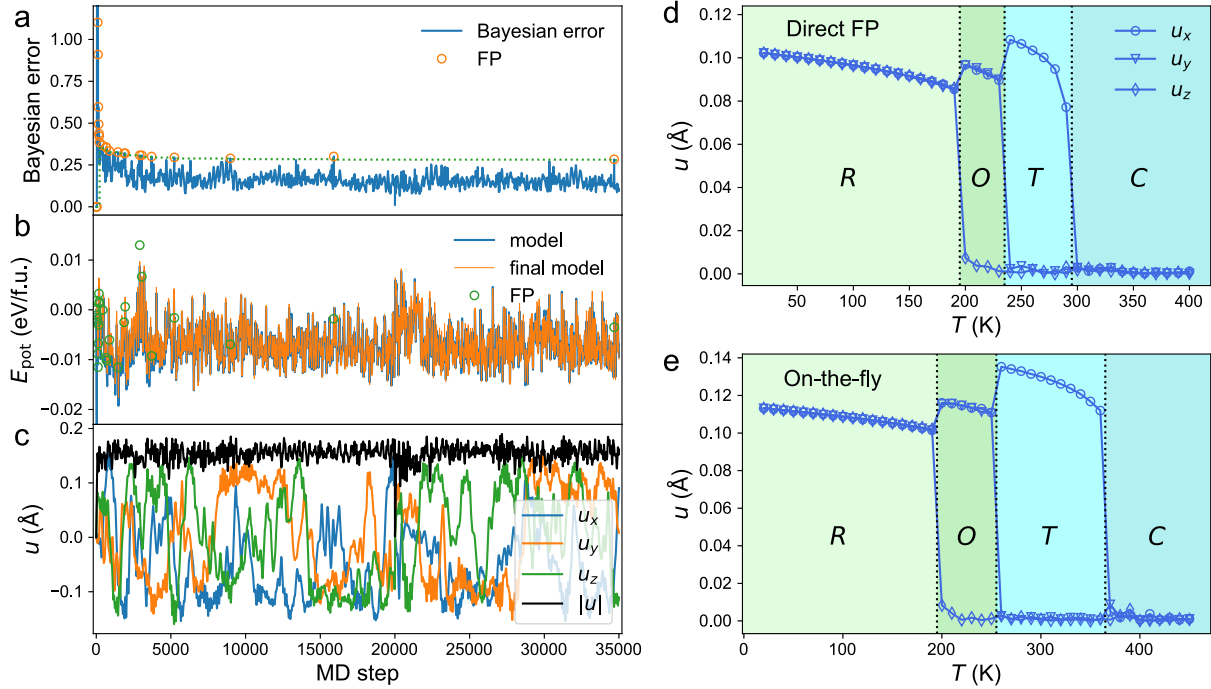


FIG. 2. On-the-fly machine learning of parametrization for BaTiO₃. (a, b, c) (a) Bayesian error, (b) potential energy per formal unit (f.u.), and (c) local soft mode u in the learning/fitting process as functions of MD steps. The dash line in panel (a) denotes the threshold to perform FP calculations. The blue and orange lines in panel (b) represent the energy computed by effective Hamiltonian model during the fitting process and with the final parameter after the learning process, respectively. Phase diagram by effective Hamiltonian simulations with the parameters from (d) FP calculations in Ref. [7] and (e) on-the-fly learning. Absolute values of local mode u of BaTiO₃ as functions of temperature are shown in panel (d) and (e). Here, R, O, T, and C denote the rhombohedral, orthogonal, tetrahedral and cubic phases, respectively.

for effective Hamiltonian. The parameters are fitted during effective Hamiltonian MD simulations on relatively small cells. As shown in Fig. 1b, in each MD step, the energy, forces and stress tensor on the structure as well as their uncertainties are predicted by the effective Hamiltonian with the current parameters and collected data using the Bayesian linear regression. If the uncertainty (Bayesian error) of the energy, forces or stress tensor is large, FP calculation is executed, the corresponding results are stored into the train set, and the parameters are fitted using the updated train set; otherwise, the FP calculation is skipped. Then, the structure is updated by executing one MD step with the forces and stress from the FP calculation (if available) or those from the effective Hamiltonian.

During the fitting process, the Bayesian error of the energy, forces and stress predicted by the effective Hamiltonian is calculated by Eq. (24) (see more details in Methods) and compared to the threshold to determine whether FP calculation is necessary. At the beginning, the threshold is typically initialized with zero. Before the setting up of nonzero threshold, the FP calculations take place in fixed interval of several steps (say, 10 or 20 MD steps). The threshold is then updated dynamically during the fitting process using the flow similar to that in Ref. [2], with the exception that the spilling factor is not used in this work. Note that different from Ref. [2], the

parameters are typically fitted *immediately* as soon as when new FP calculation is performed, instead of fitted after several FP results are obtained. This difference stems from the observation that the parameter fitting for the effective Hamiltonian is typically very fast compared to the FP calculations. Such immediate fitting is helpful for reducing the number of FP calculations required and improve the fitting efficiency.

Examples of application

The on-the-fly learning effective Hamiltonian is first applied to BaTiO₃, which is one of the most studied ferroelectric perovskite materials. BaTiO₃ is in cubic paraelectric phase at high temperature. With the decreasing of temperature, it transforms into tetrahedral, orthogonal and rhombohedral ferroelectric phases. The effective Hamiltonian of BaTiO₃ have been developed in 1994 by Zhong *et al.*, which correctly reproduces the phase transition sequence, but with lower transition temperatures comparing with experiments [7]. Several modifications have been performed on the form and/or parametrization of the effective Hamiltonian to improve its accuracy [31].

An example of the typical evolution during on-the-fly machine learning run is depicted in Fig. 2. The simulation temperature is chosen to be 50 K. Figure 2a shows the Bayesian

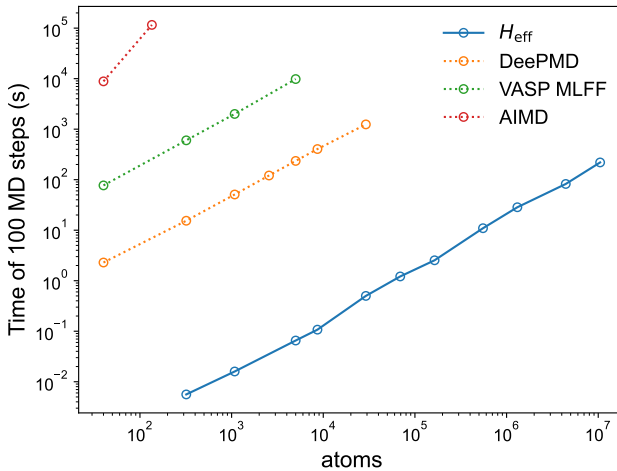


FIG. 3. Computational time for 100 MD steps calculations as a function of the number of atoms in the simulated of BaTiO_3 supercell, using the effective Hamiltonian (H_{eff}), deep potential MD, MLFF implemented in VASP, and ab-initio MD (AIMD) in VASP. The tests are performed on Intel(R) Xeon(R) Silver 4210R CPU using one core, expect for the AIMD simulation, which is performed on the Intel(R) Xeon(R) CPU E5-2680 v3 CPU using 24 cores.

error during the fitting process. At the beginning (about 500 steps), the Bayesian error is quite large, and FP calculations are called frequently. As the fitting progresses, more FP data is collected and the parameters are updated, leading to the rapid decline of Bayesian error. The threshold is also adjusted dynamically in this process. After about 1000 MD steps, the threshold is nearly unchanged and the FP calculations are only rarely required. Figure 2b shows the potential energy predicted by the effective Hamiltonian and that computed from FP calculations in the simulation, showing they are close to each other at each step. Figures 2c show the mode evolution during the simulation. At the beginning of the simulation, the soft mode u vibrates in different directions. After about 17000 steps, the average value of u shows finite values along the x, y, z directions, characterizing the rhombohedral ferroelectric phase, consistent with the ground state in experiments [12].

Figure 2d,e shows the phase transition of BaTiO_3 obtained from the MC simulations using the effective Hamiltonian with parameters directly from the FP calculations and that from on-the-fly learning. For the two simulations, the negative pressures of -4.8 GPa and -2.8 GPa are applied to partially correct the potential underestimation of the lattice constant in the FP calculations. At high temperature, all components of the soft mode are zero, characterizing an average paraelectric cubic phase. With the decreasing of temperature, the BaTiO_3 sample sequentially transforms to ferroelectric tetrahedral, orthogonal and rhombohedral phases, characterized by one, two, and three non-zero components of the soft mode, respectively. Such phase transition sequence is correctly reproduced by the effective Hamiltonian with both sets of parameters. For the

parameters from direct FP calculations [Fig. 2d], the transition temperatures of cubic-tetrahedral, tetrahedral-orthogonal and orthogonal-rhombohedral phase transitions are about 290, 230 and 190 K, comparing to the experimental transition temperatures of 403, 278 and 183 K, respectively [12]. The transition temperatures predicted by on-the-fly learning parameters are 360, 250, and 190 K, respectively, much closer to the experimental values. Such improvement of the transition temperatures may be arisen from the inclusion of anharmonic intersite interactions, such as the u^2-u^2 and u^3-u^1 convolution interactions (see “Methods”).

To demonstrate the computational efficiency of the effective Hamiltonian, the time consumed by the effective Hamiltonian, deep potential MD [32], MLFF MD and ab-initio MD simulations implemented in VASP [2] are shown in Fig. 3 as functions of the number of atoms in the simulated supercell. One can see that the time consumed by ab-initio MD simulations increases drastically with the increasing of supercell size, and is much slower than other methods, as consistent with common beliefs. The time spent by other methods increase slowly with the increasing of supercell size within similar slope in the log-log scale. For the same supercell size, the time spent by effective Hamiltonian simulation is less than the deep potential MD and MLFF MD implemented by VASP by about 3 and 5 orders of magnitude, respectively.

The second example is the halide perovskite CsPbI_3 , which is one of the promising candidate materials in cost-effective, high-performance electronics and optoelectronics [33]. An effective Hamiltonian has been developed using first-principle calculations in Ref. [11]. Figure S1 shows the phase transitions predicted by the effective Hamiltonian with parameters from direct FP calculations and on-the-fly learning, respectively. Both sets of parameters predict a direct phase transition from high temperature cubic phase to low temperature $Pnma$ phase. Note that an intermediate phase with macroscopically tetrahedral symmetry is observed in experiments [34], and as shown in Ref. [11], such intermediate phase may emerge in the effective Hamiltonian simulation by properly adjusting the k_2 parameter. The phase transitions of CsPbI_3 at finite temperature are discussed in Supplementary Information.

The on-the-fly learning approach is then applied to the $(\text{Pb}, \text{Sr})\text{TiO}_3$ system, which shows various topological polar structures. Examples are skyrmion-like nanodomains found in bilayer structures [35] and polar vortex lattices predicted in superlattices [36]. Here, the $\text{SrTiO}_3/\text{PbTiO}_3$ surface structure with relatively thick PbTiO_3 layer and thin capping SrTiO_3 layer is built, and the parameters are obtained by performing on-the-fly learning on $(\text{Pb}_{7/8}\text{Sr}_{1/8})\text{TiO}_3$ solid solutions. Figure 4a shows the local dipole configuration averaged over the top 10 PbTiO_3 layers (i.e. the 10 PbTiO_3 layers directly adjacent to the interface between PbTiO_3 and capping SrTiO_3 layer) obtained from hybrid Monte Carlo (HMC) simulations, clearly shows skyrmion-like patterns. Figure 4b shows one of the vertical slices near a skyrmion-like nanodomain. Such skyrmion-like nanodomain is further experimentally confirmed by piezoelectric force microscope (PFM)

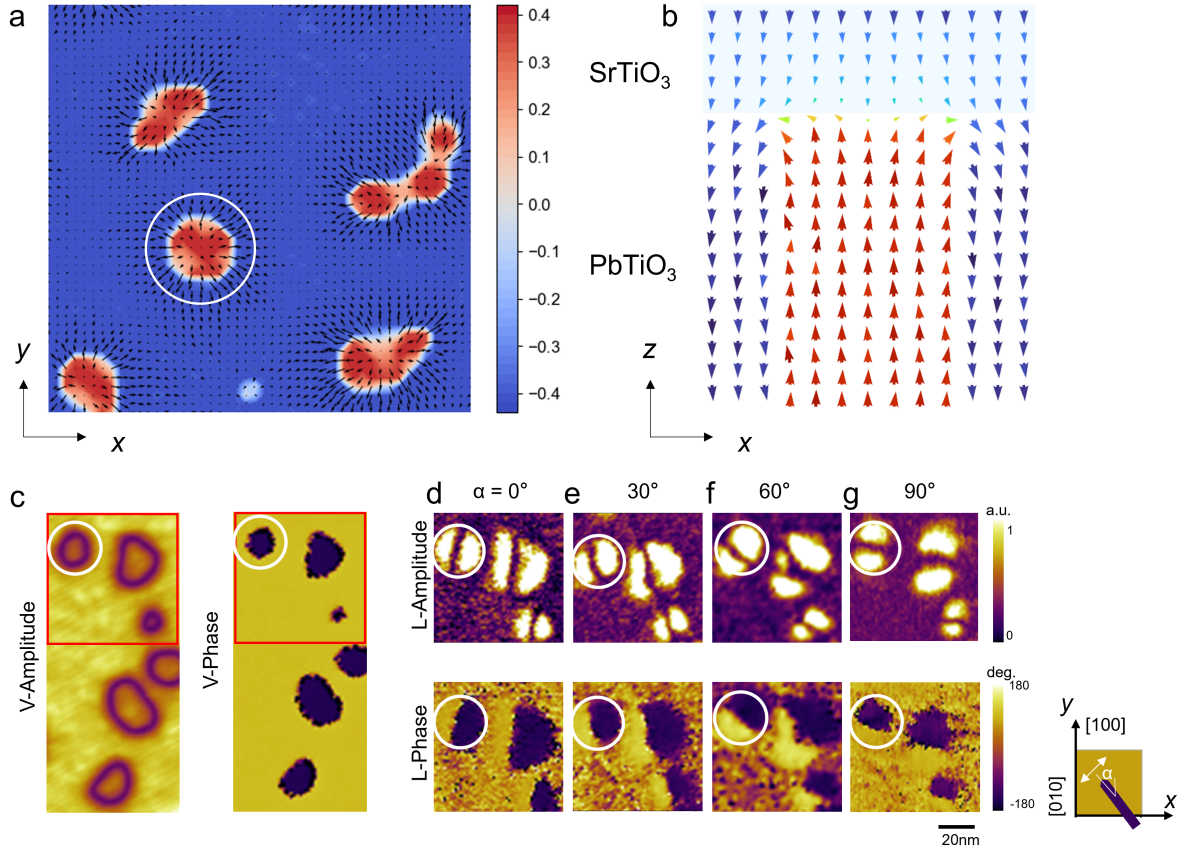


FIG. 4. Polar distribution of $\text{SrTiO}_3/\text{PbTiO}_3$ surface. (a) Dipole configuration of $\text{SrTiO}_3/\text{PbTiO}_3$ averaged over the top 10 planes of PbTiO_3 layer obtained from HMC simulation with the effective Hamiltonian. The arrows denote the in-plane component of the local soft mode, and the colors denote the out-of-plane components of soft modes. (b) The dipole configuration of $\text{SrTiO}_3/\text{PbTiO}_3$ in a (010) plane around the circled skyrmion-like domain in panel (a). The colors of the arrows denotes the out-of-plane component of local soft mode. (c-g) The PFM images characterizing the skyrmion-like domains in $\text{SrTiO}_3/\text{PbTiO}_3$. (c) Vertical PFM amplitude and phase. (d-g) Lateral PFM amplitudes and phases corresponding to the range marked with red rectangles in panel (c), with tip orientation angles of 0° (d), 30° (e), 60° (f) and 90° (g). The white circles in panels (c-g) mark one of the skyrmion-like nanodomains.

images showing in Fig. 4c-g. The consistency between our simulation and observation demonstrates the validity of our on-the-fly learning effective Hamiltonian approach in such complex system.

DISCUSSION

On-the-fly machine learning scheme is developed to obtain the parameters of the effective Hamiltonian. The parameters are computed during MD simulations. The energy, forces and stress as well as their Bayesian errors are predicted at each MD step based on the effective Hamiltonian and FP data collected before, and FP calculations are called to fit the parameter when the Bayesian errors are large. The fitting procedure based on Bayesian linear regression provides not only the values of the parameters, but also their uncertainties. For complex perovskites with multi element in A or B site, the component-dependent parameters are fit-

ted in simultaneously with other parameters, without the need of using VCA. Such learning scheme offers a new alternative to parametrize the effective Hamiltonian in a universal and highly automatic process, and is especially suitable for the systems that have complex interaction terms and/or complex components. This parametrization scheme is applied to BaTiO_3 , CsPbI_3 and $\text{SrTiO}_3/\text{PbTiO}_3$ surface. The phase transition sequences predicted by the learned effective Hamiltonian is consistent with experiments and/or previous effective Hamiltonian works. Moreover, the effective Hamiltonian of $\text{SrTiO}_3/\text{PbTiO}_3$ predicts the dipolar skyrmion-like nanodomains, which is also confirmed by experimental observation. Such demonstrations show the validity of our on-the-fly learning scheme.

METHODS

Effective Hamiltonian for perovskites

In the effective Hamiltonian of perovskites, the atomic displacement modes are (1) the local soft mode \mathbf{u}_i in each five-atom perovskite unit cell i , which is directly proportional to the local electric dipole in unit cell i [7]; (2) the pseudovector ω_i centered at B site, characterizing the BX_6 octahedral tilting, also known as antiferrodistortive (AFD) distortions [9]; and (3) the local variable \mathbf{v}_i characterizing the inhomogeneous strain around the unit cell i [7]. Note that the \mathbf{u}_i and \mathbf{v}_i vectors could be chosen to be centered at either A site or B site for different materials. As described in the main text [Eq. (1)], the potential energy of perovskites contains four main parts. Here, the first two terms E_{single} and E_{strain} contains mainly the terms already reported in previous effective Hamiltonian works (with a small amount of extension, see the Supplementary Information for more details).

The E_{conv} in Eq. (1) contains several two-body interaction terms that takes the following form

$$E_{\text{conv}}^{pq} = \sum_{ijab} p_a(\mathbf{R}_i) q_b(\mathbf{R}_j) K_{ab}(\mathbf{R}_i - \mathbf{R}_j), \quad (5)$$

where \mathbf{R}_i and \mathbf{R}_j are the position of the sites indexed by i and j , p and q are two variables participating in this interaction, a and b are their subscripts. This type of interaction is called “convolution interaction” in this work, since such form is consistent with the mathematical definition of “convolution”. The “convolution kernel” $K_{ab}(\mathbf{R}_i - \mathbf{R}_j)$ contains the symmetry and parameter of the interaction. The specific form of the convolution kernel is determined by finding the symmetry invariant terms under the symmetry operations of the reference structure (see Ref. [37]). The convolution interaction may be either long-ranged or short-ranged. For long-range interactions, both the i and j indexes run over all the sites in the simulated supercell. On the other hand, for short-range interactions, the i index runs over all the sites in the simulated supercell, while the j runs over the neighbor sites around i (within certain range for each type of interaction). In such case, the convolution kernel $K_{ab}(\mathbf{R}_i - \mathbf{R}_j)$ is localized. Note that, the convolution variable p, q here could be not only the primitive degrees of freedom (i.e. $\mathbf{u}, \mathbf{v}, \omega$), but also their onsite direct products. For example, the 6-dimension vector \mathbf{U} expressing the onsite direct product of $\mathbf{u} \otimes \mathbf{u}$ with subscript a being Voigt notation ($U_1 = u_x^2, U_4 = u_y u_z$) could be a valid convolution variable in Eq. (5). Throughout this manuscript, the expression “ $p^m - q^n$ interaction” denotes the convolution interaction that includes m th order contribution from p and n th order contribution from q . For example, the “ $u^1 - \omega^2$ interaction” is the convolution interaction that equivalent to

$$E_{\text{conv}}^{u^1 - \omega^2} = \sum_{ij\alpha\beta\gamma} u_\alpha(\mathbf{R}_i) \omega_\beta(\mathbf{R}_j) \omega_\gamma(\mathbf{R}_j) K_{\alpha\beta\gamma}(\mathbf{R}_i - \mathbf{R}_j). \quad (6)$$

As in previous MD and hybrid Monte Carlo works [38], the convolution interaction could be handled in the reciprocal space by using fast Fourier transformation to improve the computational efficiency.

Practically, the following convolution interactions are included in this work (with necessary comments followed).

(1) The $u^1 - u^1$ interaction. This is the only considered long-range interaction, which includes both the dipole-dipole interaction [Eqs (7) and (8) in Ref. [7]]

$$E_{\text{long}} = \frac{1}{2} \sum_{ij\alpha\beta} Q_{ij\alpha\beta} u_{i\alpha} u_{j\beta}, \quad (7)$$

where the summation of both i and j runs over all the sites in the supercell, and the short-range interaction [Eq. (9) in Ref. [7]]

$$E_{\text{short}} = \frac{1}{2} \sum_{ij\alpha\beta} J_{ij\alpha\beta} u_{i\alpha} u_{j\beta}, \quad (8)$$

where the i runs over all the sites in the supercell, and j runs over the neighbor sites of i (up to the third nearest neighbor).

(2) The $v^1 - v^1$ interaction, which has the same form as the inhomogeneous elastic energy E_I^{elas} in Ref. [7]

$$\begin{aligned} E_{\text{elas},I} = & \sum_i \left\{ \gamma_{11} [v_x(\mathbf{R}_i) - v_x(\mathbf{R}_i \pm \mathbf{x})]^2 \right. \\ & + \gamma_{12} [v_x(\mathbf{R}_i) - v_x(\mathbf{R}_i \pm \mathbf{x})] [v_y(\mathbf{R}_i) - v_y(\mathbf{R}_i \pm \mathbf{y})] \\ & + \gamma_{44} [v_x(\mathbf{R}_i) - v_x(\mathbf{R}_i \pm \mathbf{y}) + v_y(\mathbf{R}_i) \\ & \left. - v_y(\mathbf{R}_i \pm \mathbf{x})]^2 + \text{cyclic permutations} \right\}, \end{aligned} \quad (9)$$

where $\mathbf{x} = a_0 \hat{\mathbf{x}}, \mathbf{y} = a_0 \hat{\mathbf{y}}, \mathbf{z} = a_0 \hat{\mathbf{z}}$, and \pm indicates multiple terms to be summed. The parameters are defined as $\gamma_{11} = B_{11}^i/4, \gamma_{12} = B_{12}^i/8, \gamma_{44} = B_{44}^i/8$, where the superscript i denotes “inhomogeneous”. One can easily verify that such interaction term is inline with the convolution form in Eq. (5), and each component in the convolution kernel is a linear combination of the B_{lm}^i parameters here.

(3) Interactions of ω within 4 order up to the nearest neighbors, including $\omega^1 - \omega^1, \omega^2 - \omega^1, \omega^2 - \omega^2$ and $\omega^3 - \omega^1$ interactions. The harmonic $\omega^1 - \omega^1$ interaction are widely used in previous effective Hamiltonian works. For the other anharmonic interactions, some previous effective Hamiltonian works have used some of these terms (e.g., Ref. [39] employed one $\omega^3 - \omega$ term, Ref. [40] employed one isotropic $\omega^2 - \omega^2$ interaction), but not all the symmetry-allowed terms.

(4) Interactions of u within 4 order up to the nearest neighbors, including $u^2 - u^1, u^2 - u^2$ and $u^3 - u^1$ interactions. Note that one of the $u^2 - u^1$ interaction terms is found to be responsible to the electric Dzyaloshinskii-Moriya interaction in Ref. [41].

(5) Interactions between v and u within quadratic contribution of u and linear contribution of v up to nearest neighbor, including $v^1 - u^1$ and $v^1 - u^2$ interactions. Note that both the

cases of A-centered u (with B-centered v) and B-centered u (with A-centered v) are considered.

(6) Interactions between v and ω within quadratic contribution of ω and linear contribution of v up to nearest neighbor, including $v^1 - \omega$ and $v^1 - \omega^2$ interactions. Both the cases of A-centered v and B-centered v are considered.

(7) Interactions between u and ω within 4 order. For B-centered u (note that ω is always centered at B site in this work), only onsite interactions are considered. In this case, the interaction is rather simple, only three independent $u^2 - \omega^2$ interactions are valid, as considered in previous works [9, 39]. For A-centered u , the interactions between nearest neighbors are considered, and the resulting forms are rather complicated, which includes $u^1 - \omega^1$, $u^2 - \omega^1$, $u - \omega^2$ and $u^2 - \omega^2$ interactions, all with some valid terms. Note that the $u^1 - \omega^1$ interaction is used and found to be responsible for the antiferroelectric phase of PbZrO_3 in Ref. [42]; one of the $u^1 - \omega^2$ interaction terms is used and found to be important for the $Pnma$ phase in some perovskites [11, 39]; three of the $u^2 - \omega^2$ interaction terms (out of 8 considered in this work, which have similar forms to that in the B-centered u case) are widely used in previous works [39].

Now let us give a brief discussion about the “inhomogeneous strain” η_I introduced in previous works [7]. In previous works, the inhomogeneous strain $\{\eta_I\}$ is computed by the linear combination of $\{v_i\}$ degrees of freedom, and is treated “similarly” to the homogeneous strain η [7]. Such “similarity” could be manifested in: (i) the γ coefficients in Eq. (9) is directly related to the “homogeneous” elastic constants B_{11} , B_{12} and B_{44} [7]; and (ii) the inhomogeneous strain participates in the interactions between strain and soft mode u or AFD ω , where the “total strain” is calculated as the summation of homogeneous strain and inhomogeneous strain [7, 9]. However, in this work, they are treated separately. In fact, the inhomogeneous strain η_I is practically *not* introduced as intermediate variable in the effective Hamiltonian. First, in Eq. (9), the γ coefficients are associated with another set of parameters B_{11}^i , B_{12}^i and B_{44}^i , which are independent from the “homogeneous” elastic constants B_{11} , B_{12} and B_{44} . It is numerically found in the machine learning process that the B_{lm}^i and B_{lm} parameters can be rather different from each other, and using the approximation in Ref. [7] (i.e. letting $B_{lm}^i = B_{lm}$) may lead to large errors in B_{lm} . Second, the strain in Eq. (S5) contains only the “homogeneous strain”, but not “inhomogeneous strain”. The $\eta_I^1 - u^2$ interaction (respectively, $\eta_I^1 - \omega^2$ interaction) is actually a specific type of $v^1 - u^2$ interaction (respectively, $v^1 - \omega^2$ interaction), considering $\{\eta_I\}$ is just linear combinations of $\{v\}$. In this work, the valid interactions between v and u^2 (respectively, ω^2) within certain range are extracted from symmetry analysis. Thus, the $v^1 - u^2$ (respectively, $v^1 - \omega^2$) convolution interaction takes the place of $\eta_I^1 - u^2$ (respectively, $\eta_I^1 - \omega^2$) interaction. Such scheme treats “inhomogeneous strain” differently from the homogeneous strain, and could provide better accuracy for describing the potential landscape.

The E_{spring} term in Eq. (1) consists of several so-called

“spring” terms that take the following form

$$E_{\text{spring}}^p = \sum_{ija} p_a(\mathbf{R}_i) J_a(\sigma_j, \mathbf{R}_j - \mathbf{R}_i), \quad (10)$$

where p is a variable [like that in Eq. (5)] that can be primitive variables (u, v, ω) or their onsite direct products, and $J_a(\sigma_j, \mathbf{R}_j - \mathbf{R}_i)$ is the interaction matrix containing the symmetry and parameter information that depending on the occupation on site j and the position difference between i and j sites. To determine the specific form of J matrix, the σ variable is treated as an onsite scalar variable that invariant under any symmetry operations. Then, the interactions allowed by symmetry is found by performing symmetry operations (of the reference structure space group) on the products $p(\mathbf{R}_i)\sigma(\mathbf{R}_j)$ and found the invariant terms. Practically, the following spring interactions are considered. (1) The spring interaction of u of first, second and third order. (2) The spring interaction of v of first order. (3) The spring interaction of ω with second order. Note that considering the case of multi B-site element (i.e. the σ variables are centered on B site) and ω centering on B site, the first order of spring interaction is forbidden by symmetry. Thus, the second order interaction is the lowest order one.

Here is a brief discussion about the relations and differences between the E_{loc} employed here and that employed in previous works. There are two main types of interactions characterizing the “alloying effect” (using the terminology of Ref. [19]) that are proposed by Ref. [19] and widely used in previous effective Hamiltonian works. The first type is the intersite interaction associated with the “random electric field” or “random strain field” (which is believed to have important effect in compounds with hetero valence B-site elements [43]), which takes the form

$$E_{\text{intersite}}^u = \sum_{ij} Q_{ij}(\sigma_j) \mathbf{e}_{ji} \cdot \mathbf{u}_i, \quad (11)$$

where the summation of i runs over all the sites in the supercell, and the summation of j runs over the neighbor sites around i , \mathbf{e}_{ji} is the unit vector jointing the B site j and the center of local soft mode \mathbf{u}_i , and the intersite interaction for v takes the similar form. Comparing Eqs. (11) and (10), it is clear that Eq. (11) is a special form of Eq. (10) by substituting p with u , and let the interaction matrix $J(\sigma_j, \mathbf{R}_j - \mathbf{R}_i)$ to have the specific form $Q_{ij}(\sigma_j) \mathbf{e}_{ji}$. Moreover, it is easily verified the two expressions are *exactly equivalent* if the relative position $\mathbf{R}_j - \mathbf{R}_i$ is a vector of a high symmetry direction under the cubic reference structure (i.e. $\mathbf{x}, \mathbf{x} + \mathbf{y}, \mathbf{x} + \mathbf{y} + \mathbf{z}$ or their symmetry equivalents). The second type is the onsite contribution that takes the form (see also Ref. [27])

$$E_{\text{onsite}}^{u^2} = \sum_i \Delta\kappa_2(\sigma_i) u_i^2, \quad (12)$$

and similar expressions are adopted to the α and γ parameters for the fourth order onsite contribution. Such onsite contribution is a special case of Eq. (10) if the σ and u are centered

at the same site. One can understand this by noting that the product $\sigma(\mathbf{R}_i)u^2(\mathbf{R}_i)$ has the same symmetry as $u^2(\mathbf{R}_i)$ [i.e., for any symmetry operation \mathcal{O} , $\sigma(\mathbf{R}_i)u^2(\mathbf{R}_i)$ is invariant under \mathcal{O} if and only if $u^2(\mathbf{R}_i)$ is invariant under \mathcal{O}]. Similar results can be addressed for $u^4(\mathbf{R}_i)$ and $u_x^2(\mathbf{R}_i)u_y^2(\mathbf{R}_i)$. In other words, the term depending on $\Delta\kappa_2$ is a special term of Eq. (10) with quadratic contribution of u , and the terms depending on $\Delta\alpha$ and $\Delta\gamma$ are two special terms of Eq. (10) with quartic contribution of u . In this work, the latter (quartic one) is not considered, but could be easily added if necessary.

Note that, for a specified materials, some of the above terms may not be used since their effects are not important.

Mode and basis

The mode is the local collective displacement of atoms in a specified pattern (see Fig. 1a), which is also called lattice Wannier function (LWF) [7, 44]. In perovskites, the LWF basis of local dipole motion \mathbf{u} is typically chosen to be the local phonon mode having Γ_{15} symmetry centered on A or B site [18]. Typically, the LWF basis is determined from the eigenvector associated with the soft mode of the force constant or dynamic matrix of cubic perovskite, which takes the form $\xi = (\xi_A, \xi_B, \xi_{X1}, \xi_{X2})$. For example, the displacement of local mode motion $u_{i\alpha}$ centered at B site consists of the displacement of center B atom by amounts of $u_i\xi_B$, the displacement of eight neighbor A atom by amounts of $u_i\xi_A/8$, and the displacement of the six neighbor X atom by amounts of $u_i\xi_{X1}/2$ or $u_i\xi_{X2}/2$, all along the α direction. The local motion \mathbf{v} is similar to \mathbf{u} but with the basis corresponding to the translation motion of all the atoms in the unit cell, i.e. with $\xi_A = \xi_B = \xi_{X1} = \xi_{X2}$.

The AFD mode ω is kind of different from the \mathbf{u} and \mathbf{v} modes, since the neighbor BX_6 octahedra share the same X atom, and thus the ω modes are not completely independent from each other. The actual movement of the X atom shared by the i and j sites associated with the AFD mode is given by

$$\Delta\mathbf{r}_X = \frac{a_0}{2} \hat{\mathbf{R}}_{ij} \times (\omega_i - \omega_j), \quad (13)$$

where $\hat{\mathbf{R}}_{ij}$ is the unit vector jointing the site i and site j . By the definition of Eq. (13), there are multiple (actually, infinite) different sets of $\{\omega\}$ modes representing the same atomic structure (i.e. with the same set of atomic displacement) [45]. For example, it is clear that adding an arbitrary amount of ω_0 to all of the AFD modes does not change the displacement $\Delta\mathbf{r}_X$, since the displacement only depends on the *difference* between ω_i and ω_j . To eliminate such arbitrariness, we typically impose the following extra restrictions on the AFD vectors and its cyclic permutations:

$$\forall x_0, \sum_{i, n_x(i)=x_0} \omega_{i,x} = 0, \quad (14)$$

where i is the index of unit centered at $n_x(i)\hat{x}a_0 + n_y(i)\hat{y}a_0 + n_z(i)\hat{z}a_0$, $\hat{x}, \hat{y}, \hat{z}$ are unit vectors along the x, y, z axes, and a_0

is the lattice constant of the five-atom perovskite unit cell. The summation runs over all the sites in the same layer marked with $n_x(i) = x_0$. Note that our definition of atomic displacement [Eq. (13)] is identical to that in Ref. [45] [Eq. (1) there in], but our formalism is different from that of Ref. [45] by the extra restrictions [Eq. (14)].

It is clear from above that all of the \mathbf{u}, \mathbf{v} and ω modes are linked *linearly* with atomic displacement about the reference structure. For a periodic supercell containing $N = L_x \times L_y \times L_z$ five-atom perovskite unit cells, the relation between the modes and atomic displacements could be written as

$$\mathbf{Ms} = \mathbf{x}, \quad (15)$$

where \mathbf{s} is a $9N$ column vector containing the modes $\mathbf{u}, \mathbf{v}, \omega$ in each unit cell, \mathbf{x} is a $15N$ column vector containing the atomic displacement of each atom in the supercell, and \mathbf{M} is the matrix containing the information of LWF basis. The force acting on the *mode* could then be obtained from the chain rule

$$f_{s,i} = -\frac{\partial E_{\text{pot}}}{\partial s_i} = -\sum_j \frac{\partial E_{\text{pot}}}{\partial x_j} M_{ji}. \quad (16)$$

This equation can be written in matrix form as

$$\mathbf{f}_s = \mathbf{M}^T \mathbf{f}_x, \quad (17)$$

where \mathbf{f}_s and \mathbf{f}_x gather the forces acting on the modes and atoms, respectively.

Similar to the second-principle lattice dynamics formalism [29], the actual atom coordinates in a supercell with homogeneous strain η_H and *atomic* displacement is defined as

$$\mathbf{r}_{lk} = (\mathbb{1} + \boldsymbol{\eta})(\mathbf{R}_l + \boldsymbol{\tau}_k) + \mathbf{x}_{lk}, \quad (18)$$

where $\mathbb{1}$ is the 3×3 identity matrix, $\boldsymbol{\eta}$ is the homogeneous strain (in 3×3 matrix format), \mathbf{R}_l is lattice vector corresponding to the unit cell l , $\boldsymbol{\tau}_k$ is the coordinate of atom inside the unit cell. Thus, the stress compatible with that calculated from FP should be obtained using the chain rule

$$\sigma_m = -\frac{\partial' E_{\text{pot}}}{\partial' \eta_m} = -\frac{\partial E_{\text{pot}}}{\partial \eta_m} - \sum_{lk\alpha} \frac{\partial E_{\text{pot}}}{\partial x_{lk\alpha}} \frac{\partial x_{lk\alpha}}{\partial \eta_m}, \quad (19)$$

as described in Appendix A of Ref. [29]. Practically in this work, such relation is used *inversely*. The stress $-\partial' E_{\text{pot}}/\partial' \eta_m$ obtained from the FP calculations are converted to $-\partial E_{\text{pot}}/\partial \eta_m$, compatible with the direct definition of the effective Hamiltonian.

Bayesian linear regression

Given two necessary assumptions satisfied (see Appendix B of Ref. [2]), the posterior distribution of the parameter is a multidimensional Gaussian distribution

$$p(\mathbf{w}|\mathbf{Y}) = \mathcal{N}(\bar{\mathbf{w}}, \boldsymbol{\Sigma}), \quad (20)$$

where the center of the distribution

$$\bar{\mathbf{w}} = \frac{1}{\sigma_v^2} \mathbf{\Sigma} \mathbf{\Phi}^T \mathbf{Y} \quad (21)$$

is the desired optimal parameters, and the variance

$$\Sigma = \left[\frac{1}{\sigma_w^2} \mathbf{I} + \frac{1}{\sigma_v^2} \mathbf{\Phi}^T \mathbf{\Phi} \right]^{-1} \quad (22)$$

is a measure of the uncertainty of the parameters. Here, \mathbf{I} is the identity matrix, σ_v is a hyperparameter describing the deviation of FP data from the model prediction $\phi_\alpha \mathbf{w}$, and σ_w is a hyperparameter describing the covariance of the prior distribution of parameter vector \mathbf{w} (see Appendix B of Ref. [2] for more details).

Given the observation of the training set, the posterior distribution of the energy, forces and stress of a new structure is also shown to be a Gaussian distribution [2]

$$p(\tilde{\mathbf{y}}|\mathbf{Y}) = \mathcal{N}(\phi \bar{\mathbf{w}}, \sigma), \quad (23)$$

where the covariance matrix

$$\sigma = \sigma_v^2 \mathbf{I} + \phi \Sigma \phi^T \quad (24)$$

measures the uncertainty of the prediction on the new structure. Following Ref.[2], the diagonal elements of the second term is used as the Bayesian error. If the Bayesian error is large, the prediction on the energy, forces and stress by current effective Hamiltonian model is considered unreliable, then new FP calculation is required to fit the parameters.

The hyperparameters σ_v and σ_w are determined by evidence approximation [2], in which the marginal likelihood function corresponding to the probability of observing the FP data \mathbf{Y} with σ_v and σ_w is maximized [see Eq. (31) and Appendix C in Ref. [2]]. Practically, the hyperparameters σ_v and σ_w are calculated along with Σ and $\bar{\mathbf{w}}$ by executing self-consistent iterations at each time when FP data for a new structure is collected.

The Bayesian linear regression described above is equivalent to the ridge regression [5, 46] in which the target function

$$\mathcal{O} = \|\mathbf{\Phi} \mathbf{w} - \mathbf{Y}\| + \lambda \|\mathbf{w}\|^2 \quad (25)$$

is minimized, where λ is the Tikhonov parameter which is equivalent to σ_v^2/σ_w^2 here [5, 46]. The main purpose of imposing the Tikhonov parameter is to prevent overfitting [46]. However, in the context of effective Hamiltonian parametrization, there are only a small amount of parameters to be determined (typically several tens), while the number of values collected from FP calculations are typically much larger, which means the linear equations $\mathbf{\Phi} \mathbf{w} = \mathbf{Y}$ is greatly overdetermined. In such case, the regularization is usually not necessary. If the regularization term $\lambda \|\mathbf{w}\|^2$ in Eq. (25) is removed, the problem becomes a simple linear least square fitting, and the parameter could be simply solved by

$$\mathbf{w} = \mathbf{\Phi}^+ \mathbf{Y}, \quad (26)$$

where $\mathbf{\Phi}^+$ is the Moore-Penrose pseudoinverse of the matrix $\mathbf{\Phi}$, which could be computed by performing the singular-value decomposition of $\mathbf{\Phi}$ [47]. Indeed, our numerical tests show that the resulting parameter from such fitting without regularization is pretty close to that obtained by Bayesian linear regression. Similar observation is also reported in the context of MLFF with Gaussian approximation potential model (or its analogs) [47]. On the other hand, in effective Hamiltonian, unlike Gaussian approximation potential, the parameters in \mathbf{w} have different dimensions, and it is hard to balance the *values* between different parameters, indicating the regularization may be not suitable for effective Hamiltonian. Based on the two reasons above, in our fitting scheme, it is typically assumed that $\sigma_w \rightarrow \infty$, and thus the equivalent Tikhonov regularization parameter λ approaches zero, and the fitting scheme is equivalent to the linear least square fitting.

Computational details

On-the-fly machine learning for parametrization of effective Hamiltonian is performed on $2 \times 2 \times 2$ or $2 \times 4 \times 4$ supercells (corresponding to 40 or 160 atoms). The MD simulations are performed with isothermal-isobaric (*NPT*) ensemble using Evans-Hoover thermostat [48]. Typically, each MD simulation on a given structure is executed for 20 ps to 200 ps. For each MD step the FP calculation is required by the on-the-fly machine learning process, first-principles self-consistent calculation within density functional theory (DFT) is performed. All the FP calculations are performed using the VASP package [49] with projector augmented wave (PAW) method. The solid-revised Perdew-Burke-Ernzerhof (PBEsol) [50] functional is used. For oxide perovskites, the $3 \times 3 \times 3$ and $3 \times 2 \times 2$ k-point meshes are used for the supercells with 40 and 160 atoms, respectively, and the plane wave cutoff of 550 eV is employed. For halid perovskite CsPbI_3 , the $4 \times 4 \times 4$ and $4 \times 2 \times 2$ k-point meshes are used for the supercells with 40 and 160 atoms, respectively, and the plane wave cutoff of 350 eV is employed. The optical dielectric constant is computed using the density functional perturbation theory (DFPT) [51]. The Born effective charge of the local mode is obtained by fitting the polarization against the local mode amplitude, where the polarization is computed using the Berry phase method [52].

The finite-temperature properties are computed by Monte Carlo (MC) simulations with Metropolis algorithm [53] or hybrid MC algorithm [38] (HMC) using the effective Hamiltonian. Each HMC sweep consists of 40 MD steps. Supercells of $12 \times 12 \times 12$ (corresponding to 8640 atoms) are used, unless specially noted. For the phase transition simulations, the systems are cooled down from high temperature with relatively small temperature steps.

In the MD and MC simulations, the following quantities are computed: (i) the average soft mode defined as $\mathbf{u} = \frac{1}{N} \sum_i \mathbf{u}_i$, (ii) the average amplitude of soft mode defined as $|\mathbf{u}| = \frac{1}{N} \sum_i |\mathbf{u}_i|$, (iii) the AFD at R point defined as $\omega_R = \frac{1}{N} \sum_i \omega_i (-1)^{n_x(i) + n_y(i) + n_z(i)}$, and (iv) the AFD at

M point defined as $\omega_M = \frac{1}{N} \sum_i \omega_i (-1)^{n_x(i) + n_y(i)}$.

In the demonstration of BaTiO₃, the soft mode $\{\mathbf{u}_i\}$ is chosen to be centered at B site, the inhomogeneous strain variable $\{\mathbf{v}_i\}$ is chosen to be centered at A site, and the AFD $\{\omega_i\}$ variables are frozen at zero since they are not important in BaTiO₃. Such configuration of the degrees of freedoms is consistent with the previous work [7]. In the effective Hamiltonian, the soft mode onsite energy [Eq. (S2)] is considered up to the quartic order, the elastic energy [Eq. (S4)] is considered up to the quadratic order, and the $\eta - u$ interaction is considered only up to the first term in Eq. (S5). The PBEsol functional is used in the FP calculations. The $2 \times 2 \times 2$ and $2 \times 4 \times 4$ supercells (corresponding to 40 and 160 atoms, respectively) are used in turn for on-the-fly learning. For Fig. 3, the effective Hamiltonian simulation is conducted with one CPU core on different supercell sizes of BaTiO₃ for 10 000 steps, the average time spent by each MD step is then calculated (with the initial preparation time excluded). For each size of supercell, such process is repeated for 5 times to get the average time. The MLFF simulation is performed using the VASP [2] package. The force field for BaTiO₃ is first trained within $2 \times 2 \times 2$ supercell (40 atoms) at 300 K using 10000 MD steps. In this process, 461 local reference structures are collected. Then, it is switched to the prediction-only mode (ML_ISTART=2) using the generated force field to measure the consumed time. For each supercell size, the simulation is performed with 1 CPU core for 100 MD steps, and the consumed times by each step (excluding the first and last step) are averaged to produce the results. The deep potential MD [32] simulation is performed with the LAMMPS package with one CPU core. Five repeat simulations, each last for 1000 steps, are conducted for each supercell size, and the time spent by each MD step is averaged. All the tests above are performed on Intel(R) Xeon(R) Silver 4210R CPU using one core.

The ab-initio MD simulation is performed using the VASP package on $2 \times 2 \times 2$ and $3 \times 3 \times 3$ supercells (40 and 135 atoms, respectively) with Gamma-centered K point mesh of $3 \times 3 \times 3$ and $2 \times 2 \times 2$, respectively. For each supercell size, the simulation lasts for 100 steps. The time consumed by each step (apart from the first step) is averaged. The simulations are performed on the Intel(R) Xeon(R) CPU E5-2680 v3 CPU using 24 cores.

In the demonstration of SrTiO₃/PbTiO₃ surface, the effective Hamiltonian is fitted with (Pb_{7/8}Sr_{1/8})TiO₃ solid solutions. The local soft mode $\{\mathbf{u}_i\}$ is chosen to be centered at A site, the inhomogeneous variable $\{\mathbf{v}_i\}$ and the AFD pseudovector $\{\omega_i\}$ are centered at B site. The variable $\{\sigma_i\}$ is introduced to describe the occupation of Pb and Sr atoms at A site, where $\sigma_i = 1, 2$ denote Pb, Sr atom sit at the A site indexed by i , respectively. The LWF basis of the soft mode is obtained from fitting against the atomic distortion between ferroelectric tetrahedral phase and cubic perovskite phase. The soft mode onsite energy is expanded up to the fourth order. The spring interaction of u is considered up to the third order and the nearest neighbor, the spring interaction of v is considered up to the first order and first nearest neighbor, and

the spring interaction of ω is considered up to the second order (which is the symmetry-allowed interaction of the lowest order) and the nearest neighbor. The Pb and Sr atoms are distributed randomly in the supercell during the fitting process. The SrTiO₃/PbTiO₃ surface is modeled by $48 \times 48 \times 48$ supercell (corresponding to approximately 552960 atoms) consists of 43 unit cell layers of PbTiO₃ and 5 unit cell layers of SrTiO₃ along the z axis, where periodic boundary condition is induced in x, y axes but not z axis. Both (001) surfaces are terminated with A site layer. An epitaxy strain of -0.58% is imposed to mimic the SrTiO₃ substrate. The depolarization field is treated using the approach described in [54], and the β coefficient is chosen to be 0.992 here. The local configuration of Fig. 4a,b is obtained from a quench simulation (fast cool from 410 K to 10 K with temperature step of 100 K and 5000 HMC sweeps at each temperature).

Sample deposition

The SrTiO₃/PbTiO₃ bilayer heterostructures are deposited by pulsed laser deposition. The PbTiO₃ films, about 40 nm in thickness, were deposited on (001)-oriented SrTiO₃ substrates with 80 nm thick SrRuO₃ electrodes, followed by depositing a 2 nm thick SrTiO₃ capping layer. The SrRuO₃ electrode, PbTiO₃ film and SrTiO₃ capping layer were deposited at 660, 620, and 700 °C, respectively, using a 248-nm KrF excimer laser (COMPex Pro 205F, Coherent) with an energy flux density of 1.5 J/cm² on SrRuO₃, PbTiO₃ and SrTiO₃ ceramic targets and a repetition rate of 3 Hz. 20% excessive Pb was added into the PbTiO₃ target to compensate the Pb loss during deposition. The oxygen partial pressure for the deposition of SrRuO₃ and SrTiO₃ is 100 mTorr and for the deposition of PbTiO₃ is 80 mTorr.

PFM measurement

Ferroelectric domain structures of various SrTiO₃/PbTiO₃ surfaces were characterized at room temperature by atomic force microscope (Cypher ES, Asylum Research). NanoWorld EFM platinum/iridium-coated tips and Adama Supersharp Au tips, both 2.8 N/m in force constant, were used in PFM measurements. The ac signal applied on the tip for all the PFM measurements is 800 mV in amplitude. The samples were grounded in all the measurements. Piezoresponse phase-voltage hysteresis loops were collected in the dual a.c. resonance tracking mode. The vector PFM were conducted with different in-plane sample rotation angles to reconstruct the domain structures [55, 56].

X.M., H.C., Z.Y., Y.Y. and D.W. thank the National Key R&D Programs of China (grant NOs. 2020YFA0711504, 2022YFB3807601), the National Natural Science Foundation of China (grant NOs. 12274201, 51725203, 51721001, 52003117 and U1932115) and the Natural Science Foundation of Jiangsu Province (grant NO. BK20200262). We are

grateful to the HPCC resources of Nanjing University for the calculations.

[1] Martin, R. M. *Electronic Structure: Basic Theory and Practical Methods* (Cambridge University Press, 2004).

[2] Jinnouchi, R., Karsai, F. & Kresse, G. On-the-fly machine learning force field generation: Application to melting points. *Phys. Rev. B* **100**, 014105 (2019).

[3] Podryabinkin, E. V. & Shapeev, A. V. Active learning of linearly parametrized interatomic potentials. *Comput. Mater. Sci.* **140**, 171–180 (2017).

[4] Vandermause, J. *et al.* On-the-fly active learning of interpretable bayesian force fields for atomistic rare events. *npj Comput. Mater.* **6**, 20 (2020).

[5] Jinnouchi, R., Miwa, K., Karsai, F., Kresse, G. & Asahi, R. On-the-fly active learning of interatomic potentials for large-scale atomistic simulations. *J. Phys. Chem. Lett.* **11**, 6946–6955 (2020).

[6] Friederich, P., Häse, F., Proppe, J. & Aspuru-Guzik, A. Machine-learned potentials for next-generation matter simulations. *Nat. Mater.* **20**, 750–761 (2021).

[7] Zhong, W., Vanderbilt, D. & Rabe, K. M. First-principles theory of ferroelectric phase transitions for perovskites: The case of BaTiO₃. *Phys. Rev. B* **52**, 6301–6312 (1995).

[8] Ghosez, P. & Junquera, J. Modeling of ferroelectric oxide perovskites: From first to second principles. *Annu. Rev. Conden. Ma. P.* **13**, 325–364 (2022).

[9] Korney, I. A., Bellaiche, L., Janolin, P.-E., Dkhil, B. & Suard, E. Phase diagram of Pb(Zr, Ti)O₃ solid solutions from first principles. *Phys. Rev. Lett.* **97**, 157601 (2006).

[10] Chen, P., Paillard, C., Zhao, H. J., Íñiguez, J. & Bellaiche, L. Deterministic control of ferroelectric polarization by ultrafast laser pulses. *Nat. Commun.* **13**, 2566 (2022).

[11] Chen, L., Xu, B., Yang, Y. & Bellaiche, L. Macroscopic and microscopic structures of cesium lead iodide perovskite from atomistic simulations. *Adv. Funct. Mater.* **30**, 1909496 (2020).

[12] Zhong, W., Vanderbilt, D. & Rabe, K. M. Phase transitions in BaTiO₃ from first principles. *Phys. Rev. Lett.* **73**, 1861–1864 (1994).

[13] Nahas, Y. *et al.* Discovery of stable skyrmionic state in ferroelectric nanocomposites. *Nat. Commun.* **6**, 8542 (2015).

[14] Wang, D., Bokov, A. A., Ye, Z.-G., Hlinka, J. & Bellaiche, L. Subterahertz dielectric relaxation in lead-free Ba(Zr, Ti)O₃ relaxor ferroelectrics. *Nat. Commun.* **7**, 11014 (2016).

[15] Nahas, Y. *et al.* Microscopic origins of the large piezoelectricity of leadfree (Ba, Ca)(Zr, Ti)O₃. *Nat. Commun.* **8**, 15944 (2017).

[16] Ma, X., Yang, Y., Bellaiche, L. & Wu, D. Large electrocaloric response via percolation of polar nanoregions. *Phys. Rev. B* **105**, 054104 (2022).

[17] Choudhury, N., Walizer, L., Lisenkov, S. & Bellaiche, L. Geometric frustration in compositionally modulated ferroelectrics. *Nature* **470**, 513–517 (2011).

[18] King-Smith, R. D. & Vanderbilt, D. First-principles investigation of ferroelectricity in perovskite compounds. *Phys. Rev. B* **49**, 5828–5844 (1994).

[19] Bellaiche, L., García, A. & Vanderbilt, D. Finite-temperature properties of PbZr_{1-x}Ti_xO₃ alloys from first principles. *Phys. Rev. Lett.* **84**, 5427–5430 (2000).

[20] Walizer, L., Lisenkov, S. & Bellaiche, L. Finite-temperature properties of (Ba, Sr)TiO₃ systems from atomistic simulations. *Phys. Rev. B* **73**, 144105 (2006).

[21] Naumov, I. I., Bellaiche, L. & Fu, H. Unusual phase transitions in ferroelectric nanodisks and nanorods. *Nature* **432**, 737–740 (2004).

[22] Nahas, Y. *et al.* Topology and control of self-assembled domain patterns in low-dimensional ferroelectrics. *Nat. Commun.* **11** (2020).

[23] Das, S. *et al.* Observation of room-temperature polar skyrmions. *Nature* **568**, 368–372 (2019).

[24] Lu, L. *et al.* Topological defects with distinct dipole configurations in PbTiO₃/SrTiO₃ multilayer films. *Phys. Rev. Lett.* **120**, 177601 (2018).

[25] Yin, J. *et al.* Nanoscale bubble domains with polar topologies in bulk ferroelectrics. *Nature Communications* **12** (2021).

[26] Mayer, F. *et al.* Finite-temperature investigation of homovalent and heterovalent substituted BaTiO₃ from first principles. *Phys. Rev. B* **106**, 224109 (2022).

[27] Akbarzadeh, A. R., Prosandeev, S., Walter, E. J., Al-Barakaty, A. & Bellaiche, L. Finite-temperature properties of Ba(Zr, Ti)O₃ relaxors from first principles. *Phys. Rev. Lett.* **108**, 257601 (2012).

[28] Bellaiche, L. & Vanderbilt, D. Virtual crystal approximation revisited: Application to dielectric and piezoelectric properties of perovskites. *Phys. Rev. B* **61**, 7877–7882 (2000).

[29] Escorihuela-Sayalero, C., Wojdel, J. C. & Íñiguez, J. Efficient systematic scheme to construct second-principles lattice dynamical models. *Phys. Rev. B* **95**, 094115 (2017).

[30] Bartók, A. P., Payne, M. C., Kondor, R. & Csányi, G. Gaussian approximation potentials: The accuracy of quantum mechanics, without the electrons. *Phys. Rev. Lett.* **104**, 136403 (2010).

[31] Mayer, F. *et al.* Improved description of the potential energy surface in BaTiO₃ by anharmonic phonon coupling. *Phys. Rev. B* **106**, 064108 (2022).

[32] Zhang, L., Han, J., Wang, H., Car, R. & E, W. Deep potential molecular dynamics: A scalable model with the accuracy of quantum mechanics. *Phys. Rev. Lett.* **120**, 143001 (2018).

[33] Swarnkar, A. *et al.* Quantum dot-induced phase stabilization of α -CsPbI₃ perovskite for high-efficiency photovoltaics. *Science* **354**, 92–95 (2016).

[34] Marronnier, A. *et al.* Anharmonicity and disorder in the black phases of cesium lead iodide used for stable inorganic perovskite solar cells. *ACS Nano* **12**, 3477–3486 (2018).

[35] Han, L. *et al.* High-density switchable skyrmion-like polar nanodomains integrated on silicon. *Nature* **603**, 63–67 (2022).

[36] Wu, J., Yang, J., Ma, L., Zhang, L. & Liu, S. Modular development of deep potential for complex solid solutions. *Phys. Rev. B* **107**, 144102 (2023).

[37] Zhao, H. J. *et al.* Energetic couplings in ferroics. *Adv. Electron. Mater.* **8**, 2100639 (2022).

[38] Prokhorenko, S., Kalke, K., Nahas, Y. & Bellaiche, L. Large scale hybrid monte carlo simulations for structure and property prediction. *npj Comput. Mater.* **4**, 80 (2018).

[39] Prosandeev, S., Wang, D., Ren, W., Íñiguez, J. & Bellaiche, L. Novel nanoscale twinned phases in perovskite oxides. *Adv. Funct. Mater.* **23**, 234–240 (2013).

[40] Zhang, J., Zhang, Y., Xu, T. & Wang, J. Strain-temperature phase diagram of BaZrO₃ with antiferrodistortive distortions. *Phys. Rev. B* **103**, 014113 (2021).

[41] Chen, P., Zhao, H. J., Prosandeev, S., Artyukhin, S. & Bellaiche, L. Microscopic origin of the electric dzyaloshinskii-moriya interaction. *Phys. Rev. B* **106**, 224101 (2022).

[42] Xu, B., Hellman, O. & Bellaiche, L. Order-disorder transition in the prototypical antiferroelectric PbZrO₃. *Phys. Rev. B* **100**, 020102 (2019).

[43] Íñiguez, J. & Bellaiche, L. Symmetry breaking at the nanoscale and diffuse transitions in ferroelectrics: A comparative study of $\text{PbSc}_{1/2}\text{Nb}_{1/2}\text{O}_3$ and $\text{PbZr}_{0.6}\text{Ti}_{0.4}\text{O}_3$. *Phys. Rev. B* **73**, 144109 (2006).

[44] Rabe, K. M. & Waghmare, U. V. Localized basis for effective lattice hamiltonians: Lattice wannier functions. *Phys. Rev. B* **52**, 13236–13246 (1995).

[45] Vanderbilt, D. & Zhong, W. First-principles theory of structural phase transitions for perovskites: Competing instabilities. *Ferroelectrics* **206**, 181–204 (1998).

[46] Zhou, Z.-H. *Machine learning* (Springer, 2021).

[47] Verdi, C., Karsai, F., Liu, P., Jinnouchi, R. & Kresse, G. Thermal transport and phase transitions of zirconia by on-the-fly machine-learned interatomic potentials. *npj Comput. Mater.* **7**, 156 (2021).

[48] Ponomareva, I., Bellaiche, L., Ostapchuk, T., Hlinka, J. & Petzelt, J. Terahertz dielectric response of cubic BaTiO_3 . *Phys. Rev. B* **77**, 012102 (2008).

[49] Blöchl, P. E. Projector augmented-wave method. *Phys. Rev. B* **50**, 17953–17979 (1994).

[50] Perdew, J. P. *et al.* Restoring the density-gradient expansion for exchange in solids and surfaces. *Phys. Rev. Lett.* **100**, 136406 (2008).

[51] Gonze, X. & Lee, C. Dynamical matrices, born effective charges, dielectric permittivity tensors, and interatomic force constants from density-functional perturbation theory. *Phys. Rev. B* **55**, 10355–10368 (1997).

[52] King-Smith, R. D. & Vanderbilt, D. Theory of polarization of crystalline solids. *Phys. Rev. B* **47**, 1651–1654 (1993).

[53] Metropolis, N., Rosenbluth, A. W., Rosenbluth, M. N., Teller, A. H. & Teller, E. Equation of state calculations by fast computing machines. *J. Chem. Phys.* **21**, 1087–1092 (1953).

[54] Ponomareva, I., Naumov, I. I., Kornev, I., Fu, H. & Bellaiche, L. Atomistic treatment of depolarizing energy and field in ferroelectric nanostructures. *Phys. Rev. B* **72**, 140102 (2005).

[55] Kim, K.-E. *et al.* Configurable topological textures in strain graded ferroelectric nanoplates. *Nature Communications* **9** (2018).

[56] Kim, J., You, M., Kim, K.-E., Chu, K. & Yang, C.-H. Artificial creation and separation of a single vortex–antivortex pair in a ferroelectric flatland. *npj Quantum Materials* **4** (2019).